Chapter 4

Rolling Contact Fatigue in Ultra High Vacuum

Mike Danyluk and Anoop Dhingra

Additional information is available at the end of the chapter

http://dx.doi.org/10.5772/51194

1. Introduction

Rolling elements, such as ball bearings and races, contain surface imperfections known as asperities. The height of surface asperities may be quantified through surface roughness analyses, which assigns a Ra number related the characteristics of the surface and asperities. The depth and width of the valleys between asperities is one significant characteristic of a surface that influences wear, friction, and contact fatigue life of the rolling element.

Surface lubrication may be divided into three categories: i) full film, ii) boundary layer, and iii) mixed film and boundary lubrication (Bhushan, 1999). With full film lubrication, the film is sufficiently thick so that surface asperities do not protrude through the film and will not contact the mating surface. Boundary lubrication describes the condition in which a film is present, but load is transferred between asperity peaks on the surfaces and not the film. Mixed lubrication conditions assume that both film and asperity transmit contact load, and therefore both must be considered in the analysis. A numerical approach capable of modeling all three types using fluid lubrication may be found in (Hu and Zhu, 2000). The proposed model is found to work well over a specific range of film-thickness-ratios and surface RMS roughness.

The need to quickly determine the fatigue life of rolling elements has given rise to rolling contact fatigue test methods that enable fatigue testing at reduced cost. Historically, RCF tests have used petroleum-based liquid-lubricants, which restrict rotational speed of the test due to liquid-lubrication churning. In comparison, RCF testing using solid film lubricants in ultra-high vacuum enables higher rotational speeds leading to test results in less time. For example, a rod composed of a candidate bearing material may accumulate over 10 million stress cycles in a few days running at 130Hz in ultra-high vacuum. The exact number of stress cycles accumulated on the rotating elements will depend on the specifics of the test configuration, such as ball diameter, rod diameter, and the number of balls present. In contrast, RCF testing in air using oil based liquid-lubrication is speed limited, usually to 60 Hz or less, and is limited to a maximum of three ball-contact elements. RCF testing in air using liquid-lubrication requires more time to accumulate the same number of stress cycles.

Rolling contact bearings may have multiple and diverse layers of gaseous molecules accumulated on their surface that can significantly influence friction and wear behavior. Physisorption and chemisorption of external molecules on to the substrate surface effect wear and friction, particularly for thin-films used in high vacuum conditions. Surface texture has a significant influence on wear and friction behavior as well since it determines the nature of contact. Physisorption layers of atoms involve weak Van dar Waals bonds. These layers can begin to detach from the substrate at pressures below 10^{-4} Pa in a process described as surface out-gassing. The energy to initiate physisorption outgassing is roughly 1-2 kCal/mol. Physisorbed layers of atoms do not share electrons with surface atoms and therefore may be easily removed when heat is applied in vacuum conditions. Chemisorbed layers however do share electrons with surface atoms and these bonds can be very strong with an associated energy of 10-100 kCal/mol. Physisoption occurs on all surfaces when exposed to air while chemisorption requires a chemical reaction with the substrate surface and is therefore heavily influenced by surface chemistry.

Hertzian contact analysis considers the deformation of two elastic solid surfaces with the following assumptions: i) the surfaces are smooth, continuous, and nonconforming to each other, ii) the strains are small in the contact area, iii) each solid can be modeled as an elastic half space in the proximity of the contact, and iv) the surfaces are frictionless. The two contacting surfaces can be of general shape, but most often they are chosen to be convex. Maximum shear stress occurs below the surface in the location of the contact. The depth of maximum shear stress is related to the radius of curvature and Poisson ratio of the substrate material. For example, Hertzian contact analysis applied to a material with Poisson's ratio of 0.3 is calculated to have maximum shear stress at a depth of 0.48 times the radius of the contact. Maximum compressive stress occurs at the point of contact. Maximum tensile stress takes place just beyond the edge of the contact area on the surface. Considering RCF loading conditions, subsurface cracking that eventually leads to surface spall and flaking begins at the location of maximum shear stress below the surface of the ball. If a thin film is present, an interfacial spall may result at the location of either maximum compressive or tensile stress, while subsurface cracking will occur within the substrate below the contact zone.

Understanding wear and friction requires knowledge of the type of contact between the two solid bodies. Incipient sliding occurs when two contacting bodies are pressed together such that a stick-point exists within the contact area and materials from each body slide relative to each other about that point. There is no imposed relative motion between the bodies during incipient sliding condition, rather sliding occurs due to elastic deformation of each surface around the stick-point. Friction between rolling contact elements is proportional to the shear strength of the base materials. Stresses in the contact area greater than the yield stress of the material are possible due to compression at the point of contact.

One of the benefits of solid lubricant coatings such as silver, lead, gold, and MoS_2 is their low shear strength to reduce subsurface stresses during incipient sliding. The compliant nature of these solid film lubricants helps to reduce subsurface stress by reducing shear loading in the substrate. However, if increased wear resistance is desired, then a hard and stiff layer is preferred which presents a trade-off when selecting a coating system: soft

compliant layer to reduce subsurface stress, or, a hard and stiff layer to increase wear resistance. The effective hardness of a thin solid film system is influenced by the hardness of its layers and substrate along with the elastic-plastic behavior of the coating system. If the film is very thin then the effective hardness is mostly influenced by substrate hardness, leading to an optimized lubricant coating that is thin and soft, applied over a hard-stiff coating bonded to the substrate. The soft lubricant reduces subsurface stress and the hard and stiff coating increases wear resistance.

Solid to solid contact results in two broad categories of surface bonding: adhesive and cohesive. Cohesive bonding takes place in the bulk material and has chemical interactions with covalent bonding, metallic bonding, and ionic and electrostatic bonding. Adhesive bonding involves two dissimilar surfaces and includes physical interactions and Van der Waals bonding. Adhesion is a function of material combination, crystal structure, surface condition, ambient temperature, and crystallographic orientation. Indeed, good adhesion is desired between the solid film lubricant and the surface of the rolling element, and very little cohesion is desired within the solid lubricant itself to reduce friction.

The technology of solid lubricants grew rapidly during the 1960s and 70s to meet the needs of the aerospace industry and for operation in ultra-high vacuum environment. Silver, gold, and lead along with compounds like MoS_2 and graphite were needed for environments in which liquid oil-based and hydrocarbon out gassing could not be tolerated, such as, rotating devices within very high electrical potential or inside space satellite guidance equipment. Test equipment used to gather tribology data for solid lubrication systems were developed through NASA, and industry leaders such as Timken, Du Pont, and General Dynamics to name a few. Platforms were developed for high vacuum and high temperature applications that involved sliding-contact, rolling-contact ball bearings, metal disk and riders, and sliding contact of a sleeve on a cylindrical rod and may be found in (NASA SP-5059, 1972). Each of these test platforms was designed to test a specific load situation.

Solid lubricants find unique application in systems with an operating pressure range of 10^{-4} to 10^{-9} Pa and are also temperature resistant in high vacuum. Rotating anode x-ray tubes that use ball bearing elements are one example of a rolling contact configuration under high vacuum and at high temperature. Non-volatile thin-film lubrication is required due to operation in vacuum and in the presence of high electrical potential. Solid lubrication systems are greatly influenced by process history and operating conditions. It is strongly suggested that testing and evaluation involving any solid film be done using equipment known to correlate with the specific application for which the coating system is being considered. RCF testing of coating systems and ball-bearing materials is one example of a test method that closely simulates rolling element bearing systems.

1.1. Current research

Matthews et al. (2007) report that thin film coating survival is most dependent on adhesion and substrate subsurface bonding. Surface studies at the nano scale suggest that friction begins at the atomic level through mechanical vibrations within the lattice structure of the

substrate. Substrate material properties influence spall behavior and RCF life as well. Micro-tribology considers the mechanics of cracks and fracture in the material at the asperity level. Berthier et al. (1989) consider velocity differences between contact surfaces and suggests four mechanisms to accommodate these differences: elastic deformation, fracture, shear stress, and rolling contact. They report that although hard coatings are preferred for wear resistance, the addition of a thin compliant film that includes nano scale hard elements in the solid lubricant reduces friction as well.

Sadeghi et al. (2009) report that subsurface failures usually occur during RCF testing due to fatigue. If a rolling element such as a ball-bearing is kept lubricated and clean, then the primary failure mode will be subsurface spall from fatigue. Fatigue failure beneath the substrate surface is thought to proceed as follows: i) work hardening, ii) elastic response, iii) material softening leading to yield. In a solid lubrication system that uses silver for example, work hardening of the substrate occurs within the run-in period in addition to silver transfer between the surfaces. If there is a sufficient amount of silver, the test will operate in the elastic response regime for as long as the silver is present. Material softening results in a larger volume of material that has yielded plastically. Plastic yielding begins the onset of subsurface cracking which then propagates to the surface resulting in a spall. Cracks and the onset of spall may also originate from inclusions or material defects, which, helps to explain the huge scatter in RCF life test data.

Polonsky et al. (1998) confirm two types of RCF failures related to composite coatings: subsurface-initiated spall and near-surface coating failure. They report coating-cohesive failure of 750 nm thick TiN running against softer 12.7 mm diameter ANSI M50 steel balls due to interface initiated spall in the TiN coating. Rosado et al. (2010) sought more understanding of the spall growth process once a spall has occurred and identify material parameters to optimize and improve spall growth resistance. For contact stress of 2.41 GPa, they report slower spall growth in ANSI M50 compared with either ANSI M50NiL or ANSI 52100 due to material composition and processing. Danyluk and Dhingra (2011) observe two types of failures related to RCF testing in ultra-high vacuum: coating depletion and surface spall. Solid film nickel-copper-silver lubrication was applied to ball bearings over a range of process voltage and pressure using a physical vapor deposition ion plating process. Coating depletion and surface spall failures were the two most common failure modes, and a unique spall-related non-precession type failure was also observed. The non-precession failure mode was associated with higher process voltages and with reduced RCF life.

Higgs and Wornyoh (2008) use conservation of mass to model an in-situ mechanism for self replenishing powder lubrication on sliding contacts. Application of Archard's wear law and a third-body concept are used to formulate the conservation mass equation. The control-volume-fraction-coverage (CVFC) model concept is applied to set the bounds of their theoretical approach. Wornyoh and Higgs (2011) extend the work of (Higgs and Wornyoh, 2008) to an asperity-based fractional coverage (AFC) model derivation and analysis. The latter AFC model extends the surface applicability to tribo-surfaces using atomic force microscopy that enable inclusion of surface topology information in the film transfer model.

1.2. Chapter overview

A review of the current literature indicates that ball-on-rod RCF testing in high vacuum and at high speeds (approaching 130 Hz) has not received much attention; the work presented here is meant to fill that gap related to high speed RCF testing of tribology coatings. A third-body approximation that accounts for coating wear has been implemented as well for aid to predict test life based on contact stress. A Lundberg-Plamgren empirical model is also presented for comparison with the third-body approximation model. Surface and coating diagnostic tools are presented to show the relationship between coating composition and RCF life.

2. Experimental procedure

The RCF test rig in Figure 1 was assembled using off the shelf components purchased from leading vacuum and mechanical equipment vendors (Danyluk and Dhingra, 2012a). For example, a Kollmorgen™ servo motor (model number AKM21E) is used to rotate the rod. The drive motor is mounted underneath the chamber and motor torque is delivered to the test rod inside the vacuum chamber using a ferro-fluidic rotary feed-through device similar to Kurt J. Lesker Vacuum™ part number FE121099. High vacuum is applied using a Varian™ V-81M turbo pumping system as shown in the right panel of Figure 1.

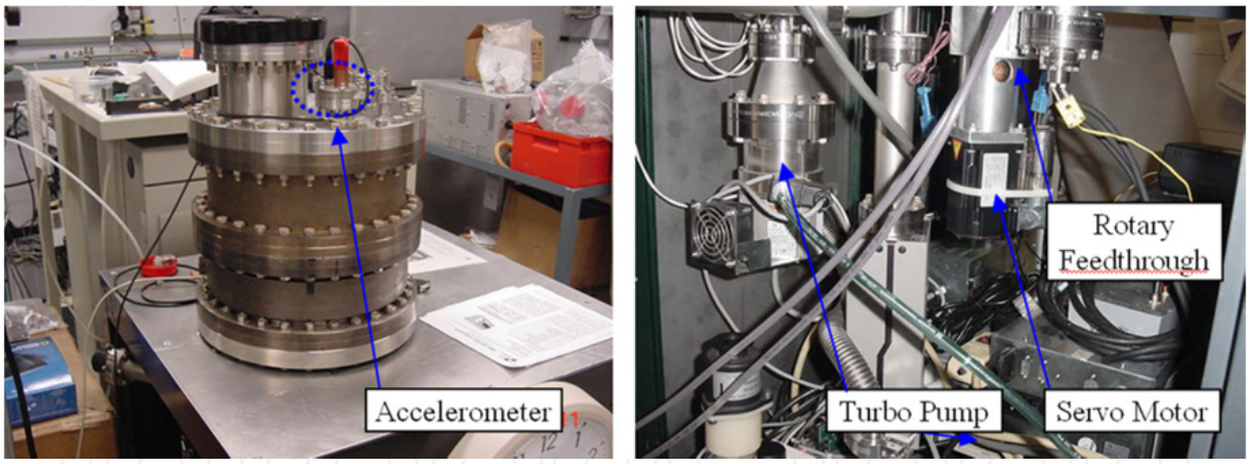

Figure 1. Support hardware and UHV-RCF chamber: turbo pumping system, residual gas analyzer, servo motor drive, and ferro-fluidic rotary feed through.

The RCF hardware inside the chamber is a modification of the three-ball-rod test rig of reference (Hoo 1982). The test-head hardware components were fabricated from 304L stainless steel and are positioned inside the UHV chamber as shown in Figure 2c. A component view of the test chamber is shown in Figure 2a, with emphasis on hardware type and assembly order. The RCF test elements: the balls, rods, and races, are shown in Figure 2b. The races are press fit into the test fixture and held stationary while the balls rotate between the fixed races and the rotating rod. A typical test consumes 5 or 6 balls depending on which ball size is used: 12.7 mm or 7.94 mm. For example, when testing with 12.7 mm diameter balls as shown in Figure 2c, five balls, two races and one rod will constitute a test.

If 7.94 mm balls are used then six balls are required. A description of test element combinations that may be carried out using this platform is presented in Table 1.

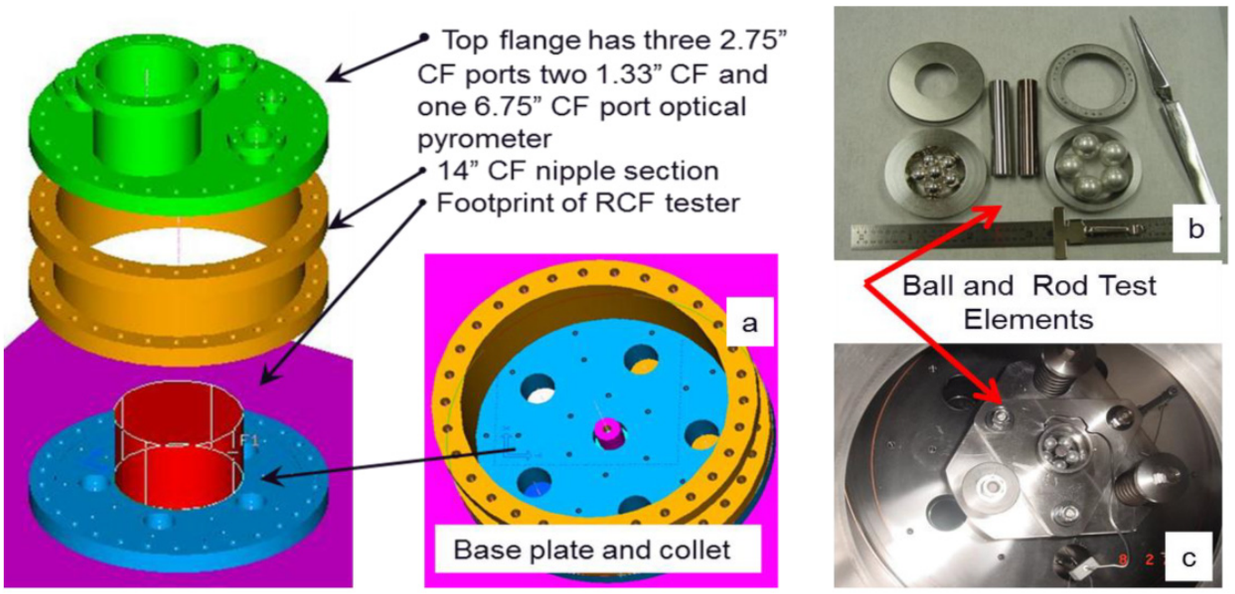

Figure 2. RCF test chamber and hardware: a) chamber sections assembly order, b) Rex 20 and M50 balls, races and rods, c) M50 balls against a Si_3N_4 rod with M50 outer races inside the vacuum chamber.

Referring to Table 1, the Si_3N_4 rods were purchased from Ceradyne™ Inc, and were processed using the EKasin™ method from Ceradyne. These rods were chosen for their high temperature and high thermal shock resistance. The Rex20 rods and races, along with the 12.7 mm diameter M50 steel balls were purchased from Timken™ and are used extensively for RCF testing with oil based lubrication. The 7.94 mm diameter ANSI T5 balls were purchased from Koyo™.

Config.	Ball Material	Rod Material	Race Material	Lubrication	Ball Size (mm)	Number of balls
1	M50 Steel	Rex 20	M50 Steel	Silver	12.7	5
2	ANSI T5	Rex 20	Rex 20	Ni/Cu/Ag	7.94	6
3	M50 Steel	Si_3N_4	M50 Steel	Silver	12.7	5

Table 1. Test configurations for RCF testing of test elements shown in Figure 2b in ultra-high vacuum.

2.1. Test material measurements

Coating survival and RCF test life is dependent on coating and substrate material properties. For example, a thin film deposited onto an M50 Steel substrate is likely to spall if the applied contact stress during the RCF test exceeds the ultimate strength of the substrate. When considering the ultimate strength and hardness of rolling bearing elements it is best to directly measure surface hardness and then approximate the ultimate strength. Substrate

geometry influences surface hardness and it is to be expected that ball, rod, and race geometries will influence the hardness measurement as well. Table 2 presents hardness and material property data for the test elements presented in Figure 2b. Table 3 contains measured surface roughness data. When collecting hardness and surface roughness data, it is recommended to carryout repeated measurements over multiple samples. For example, the data presented in Tables 2 and 3 were repeated three times per sample on five samples and the average was taken based on 15 measurements of each test element.

Material Property	9.53 mm Diameter Rex 20 Rod	9.53 mm Diameter Si_3N_4 Rod	7.94 mm Steel ANSI T5 ball	12.7 mm Steel M50 ball	Rex 20 Race	M50 Race
HRC (measured)	63.2	74.7	61.3	61.9	65.8	44.1
Elastic Modulus (GPa)	235	310	214	203	235	203
Poisson Ratio	0.29	0.25	0.29	0.29	0.29	0.29

Table 2. Hardness and material property data for RCF test elements in Figure 2b.

12.7 mm M50 Ball	M50 Race	7.94 mm T5 Ball	Rex20 Race	9.53 mm Si_3N_4 Rod	9.53 mm Rex20 Rod
0.31	0.32	0.04	0.15	0.05	0.11

Table 3. Average surface roughness Ra data in microns for RCF test elements.

2.2. Test preparation

Preparation and process history of the test elements have significant influence on RCF life. Thin film coatings on the order of 500 nm thick are very susceptible to surface contamination from exposure to air, or contact with volatile substances such as organic compounds along with low melting temperature metals such as tin or indium for example. Component cleanliness and honest adherence to good vacuum procedures are required to ensure validity of test results. For example, prior to silver deposition all of the balls were cleaned in an ultrasonic bath in methylene chloride for 20 minutes to remove oil and particulates. Prior to coating, the balls were also outgassed inside a UHV chamber at 10^{-7} Pa for 24 hours and then scrubbed with argon plasma before approximately 200 nm of silver was deposited on to the ball surface. Steps were taken to insure even coating thickness during deposition. The rods and races were cleaned similarly and all test components were stored in warm dry nitrogen. Pre-coated T5, 7.94 mm diameter balls that were purchased from Koyo were vacuum-packed and then stored in warm dry nitrogen until loaded into the test rig. Each time the test elements are exposed to air an out-gassing procedure should be applied prior to the start of the test. For example, after the balls and rod were loaded into the UHV-RCF test chamber, the system was outgassed for 12 hours at 10^{-7} Pa prior to starting the test.

2.3. Failure criterion

Based on previous testing using the RCF rig in Figure 1, the onset of a spall on at least one ball is detectable over a vibration range of 0.22 g to 0.35 g with the accelerometer mounted on the top section of the test chamber. To be clear, each test chamber may have different vibration transmissibility based on its assembly. Therefore a new test rig should be characterized for the first detectable vibration of the onset of coating spall, and verified by post-test autopsy. The failure threshold for the rig presented in Figure 1 is 0.35 g, as measured by an accelerometer mounted on the top section. For the first 15 minutes of the test, a run-in period occurs and the vibration can reach 0.30 g, then settles to a steady state range of 0.06 g to 0.15 g for length of the test until failure. The test fixture temperature measurement shown in Figure 2c tends to increases with vibration and in general tended to increase over the length of the test. This is to be expected since as the test proceeds the solid lubrication is depleted and there is an increase in surface friction and ultimately increased vibration. Temperature at failure may vary based on coating system and contact stress loading. For the test rig shown in Figure 2c a thermocouple has been placed in contact with the top race to monitor temperature during the test. An optical temperature measurement may be taken as well from the large port in the top section.

2.4. Thin film diagnostics

Confirmation of thin film composition and thickness prior to RCF testing can give insight and predictability to the test results. RCF test results may be confounded due to unknown and unwanted constituents within the coating. Auger Electron Spectroscopy (AES) may be used to measure and sample atoms within the coating. The AES process uses a high energy electron beam to bore a small diameter hole, on the order of 1 – 2 nm, into the coating and ball surface. The material that is removed during the process is analyzed using an in-situ mass spectrometer to determine its species. Figure 3 presents constituent information related to a thin film of silver that was deposited onto a 7.94 mm diameter ANSI T5 steel ball. Starting from the left, which correlates to the surface of the coated-ball, carbon, oxygen, and silver are present in the coating. Moving to the far right in Figure 3, there is a strong transition from silver to iron and chromium, which are two constituents of T5. Based on the known composition of T5 and the AES results of Figure 3 the coating thickness may be approximated as 190 nm. More interesting however is the composition of the coating through its thickness, specifically, the iron, oxygen, and nickel present throughout the silver layer. The results of Figure 4 illustrate element composition of a nickel-copper-silver coating deposited on to a Si_3N_4 ball using a physical vapor deposition ion plating process. Referring to Figure 4, there is a high concentration of nickel and iron near the ball-coating interface at about 120 nm. Since the ball itself does not contain Ni or Fe, the presence of those elements and their concentrations suggest that contamination occurred during the deposition process. The results of Figures 3 and 4 suggest interlayer mixing and coating contamination during the deposition process which is likely to influence the lubrication properties of the film, and ultimately the RCF life. For more information concerning thin film diagnostics and deposition plasma diagnostics related to RCF life, see (Danyluk and Dhingra, 2012b).

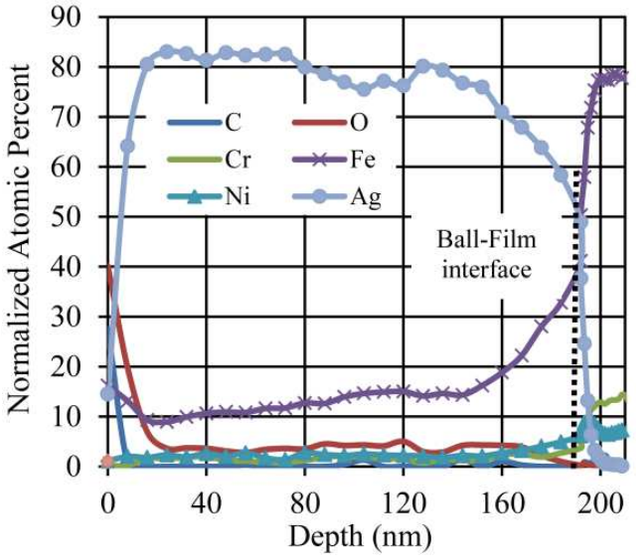

Figure 3. Auger electron spectroscopy depth profile of a silver film deposited on a 7.94 mm diameter ANSI T5 steel ball.

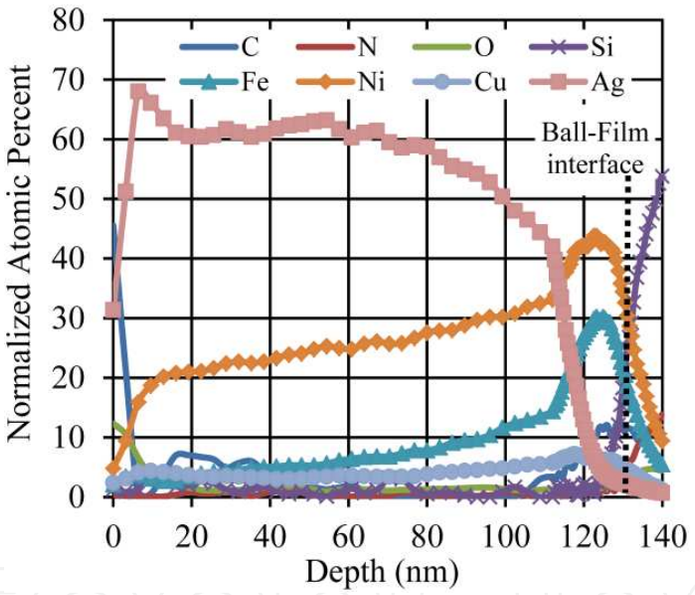

Figure 4. Auger electron spectroscopy depth profile of a nickel-copper-silver film deposited on a 7.94 mm diameter Si_3N_4 ball.

3. Experimental results

Statistical tools may be used to extract necessary information from RCF data. For example, Weibull analysis and high-cycle fatigue software tools such as Reliasoft™ may be used to correlate and compare test results independent of the coating and test elements in the test. An inverse power law life model with Weibull distribution may be used to check the experimental setup by comparing the Weibull parameters against known test configurations. Historically, a Weibull shape factor in the range $1 < \beta < 4$ is to be expected for bearing and gear type RCF failures. For comparison, a shape factor less than 1 would

indicate a flawed test method or infant failure. It is good practice to fit the RCF data to a Weibull distribution model starting after the fifth test so that one may confirm right away that the test results reflect coating and material performance and not a flawed assembly process or inadequate test preparation.

3.1. RCF statistical data

Cycles versus contact-stress for two RCF test loads using configuration 3 is presented in Figure 5. The shape factor shown in the legend of Figure 5 is within the expected range for bearing and gear type RCF testing and therefore the results reflect true film/coating performance. An eta-line has been added as well for extrapolation to testing at stress levels between the data presented in Figure 5. The shaded areas represent the fitted probability density function (PDF) based on the RCF data at that stress level.

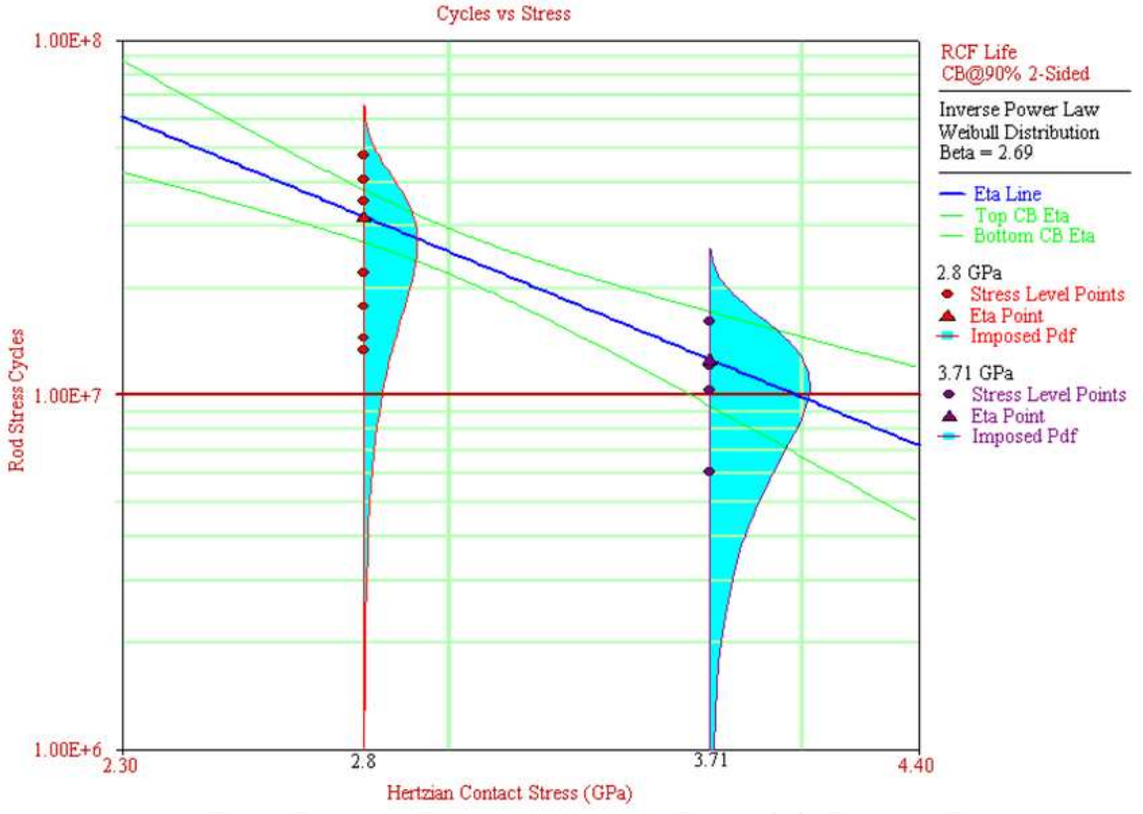

Figure 5. Cycles versus stress for 12.7 mm M50 steel balls with M50 races against a Si_3N_4 rod. Test rotation of 130 Hz in high vacuum with approximately 200 nm of silver on the balls.

Figures 6 and 7 contain reliability prediction information for two thin film systems: evaporated silver and, ion plated nickel copper silver. The Weibull shape factor for each set of data in Figures 6 and 7 is shown in the upper right corner as 2.54 and 2.76, respectively. These beta-factors are within the expected range for bearing RCF testing and therefore the data is an accurate representation of coating and rod performance. The stress-use parameter used in the reliability calculation is also presented in the figures. The stress-use parameter is a modeling tool used to extrapolate reliability data to a loading other than those actually

tested. When choosing the stress-use parameter, make sure the data is collected over a sufficient range of contact stresses that includes the stress-use value. The data presented in Figures 6 and 7 was taken over a stress-use range of 1.4 to 3.5 GPa. The results in Figures 5 through 7 strongly suggest rolling contact fatigue failure since the contact stresses for each of these tests are 1/3 less than the calculated tensile yield strength of each component as calculated from the hardness measurements presented in Table 2.

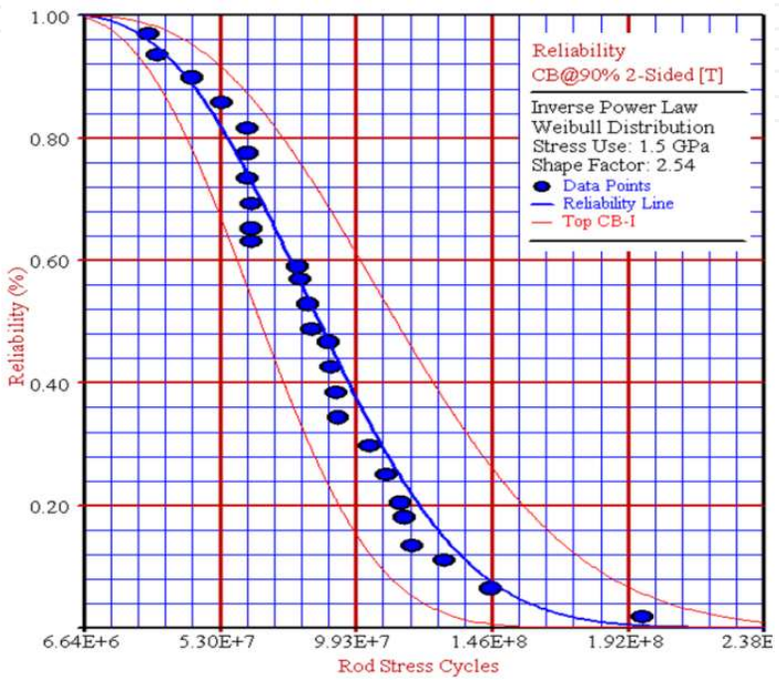

Figure 6. Reliability data for RCF elements in configuration 1 of Table 1.

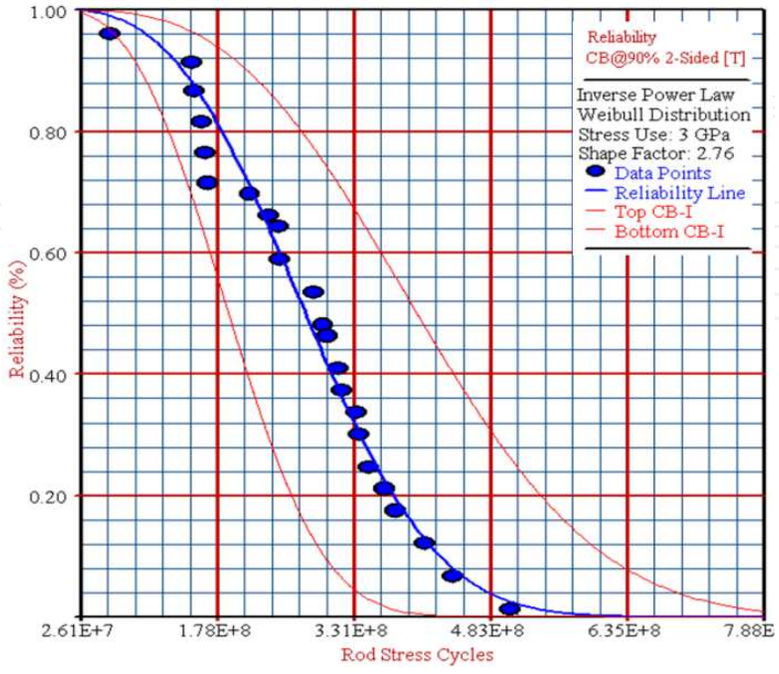

Figure 7. Reliability data for RCF elements in configuration 2 of Table 1.

3.2. RCF post test autopsy

Figures 8 through 10 present post-test photos of the ball, rod, and races for two types of failures and for two RCF loads. Configuration 1 of Table 1 was used for all three tests. Figure 8 contains results from a suspended test after 1.7 hours. A ball-rod-race model is presented in the center panel of Figure 8 to highlight the silver and the wear tracks on the ball and rotating rod. Inspection of the ball surface reveals that silver is still present on the ball surface, as illustrated by the scratch-test results shown in the right panel of Figure 8. Inspection of the rod surface shows traces of silver transfer to the rod wear track. Figure 9 contains results from a life test that eventually failed for silver depletion after 20.6 hours of testing, corresponding to 9.6 x 10^6 stress cycles accumulated on the rod wear track. Information related to silver transfer and the movement of silver on the wear track is highlighted as in Figure 9. The significance of silver transfer from the ball surface to both the rod and race wear-tracks suggests that a third-body-transfer model may be used to model the UHV-RCF test method. Concerning the rod and race information in Figure 9, the solid silver lubricant was depleted by incipient sliding between the rod-ball and race-ball contacts such that all of the silver was transferred out of the third-body storage areas. For the RCF platform, the third-body storage areas may be represented on the rod and race wear tracks.

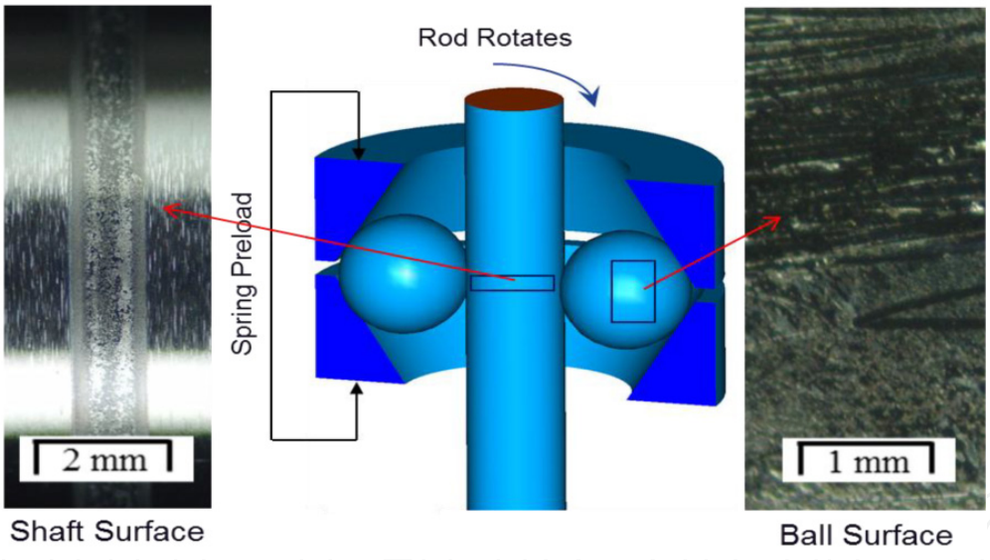

Figure 8. Autopsy data for RCF elements in configuration 1 of Table 1 operated at 3.61 GPa loading. Suspension after 1.7 hours of rotation at 130 Hz, accounting for approximately 7.8 x 10^5 rod stress cycles.

Figure 10 contains an early life spall failure of the silver coating and subsequent damage to the ball and rod surfaces. Enlargement of the rod wear track is to be expected for this failure mode since plastic yielding has occurred due to increased friction associated with spall failures. Once a coating spall occurred on at least one of the balls, the surface is damaged due to yielding and the resulting contact area with the rod increases rapidly. The test is halted after the stopping criteria, vibration levels in excess of 0.35 g, is exceeded for 1 minute. With the rod rotating at 130 Hz and a deceleration time of about 3 seconds, approximately 390 rod-rotations will be added to the failed surfaces before the rod stops

rotating. The debris from the spall remains within the wear track resulting in significant plastic deformation of all contact surfaces before the test is stopped. Coating spall failure resulted in higher friction and stress leading ultimately to surface yielding. The silver depletion failure mode resulted in increased friction and vibration as well but without surface yielding before the test was stopped. However, if allowed to continue without lubrication the increased friction would accelerate the onset of subsurface spall of the ball and rod.

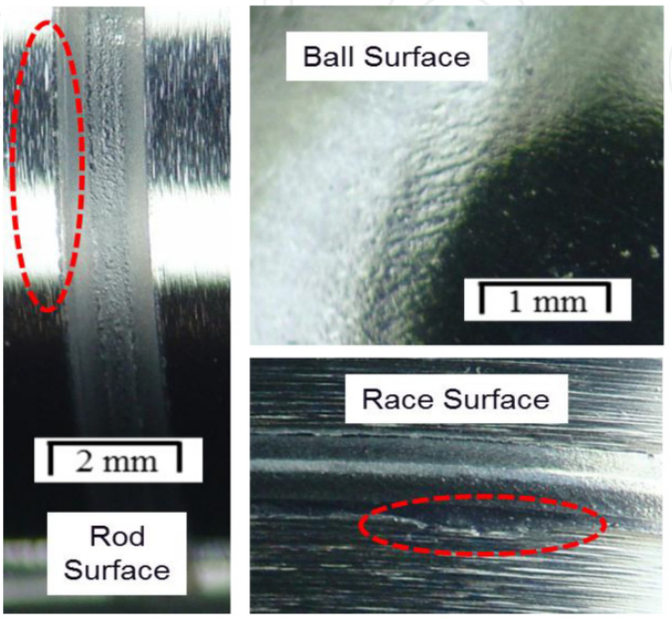

Figure 9. Autopsy data for RCF elements in configuration 1 of Table 1 operated at 3.61 GPa loading. Silver depletion failure after 20.6 hours of rotation at 130 Hz, accounting for approximately 9.6 x 10^6 rod stress cycles.

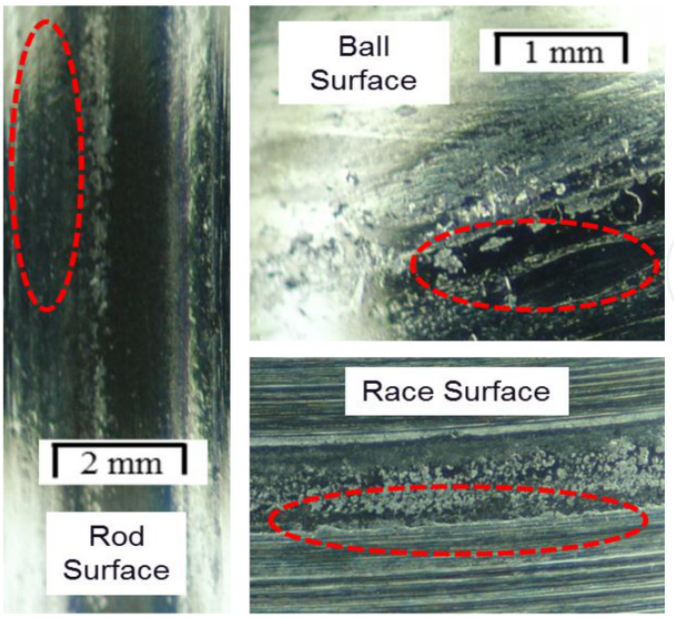

Figure 10. Autopsy data for RCF elements in configuration 1 of Table 1 operated at 4.0 GPa loading. Coating spall failure after 9.1 hours of rotation at 130 Hz, accounting for approximately 4.2 x 10^6 rod stress cycles

Post-test autopsy and Scanning Electron Microscopy (SEM) results may be used to approximate the amount of silver remaining on the ball surface at the end of each test. Table 4 presents element composition of one non-coated and two silver coated balls after testing. These balls account for three types of SEM test results: before coating, after silver depletion failure, and after early spall failure. The surface composition of each ball was derived from energy spectroscopy analyses attached to the SEM instrument. Concerning Table 4, post-test SEM data from a silver depletion failure is shown in column 3 with no silver present. All of the silver was transferred from the ball surface on to the rod and race surfaces, representing termination of the third body transfer mechanism suggested in (Higgs and Wornyoh, 2008). The results of column 4 however show some silver was still present on the ball surface following early spall failure after 9.1 hours. A theoretical analysis for a third-body transfer model using UHV-RCF data collected from suspended tests is presented in the next section.

	Baseline M50 Bearing Steel	SEM 12.7 mm M50 ball, silver depletion failure.	SEM 12.7 mm M50 ball, early spall failure.
Carbon	0.97		
Chromium	4.18	1.58	2.07
Iron	88.60	97.84	77.83
Manganese	0.32		
Molybdenum	4.45		
Silicon	0.27	0.48	0.68
Vanadium	1.21		
Silver	0.00		16.37

Table 4. Element composition of one non-coated ball and two coated balls after testing. Composition derived from energy dispersive spectroscopy using a SEM.

4. Thin film solid lubrication modelling

Test life comparison using two modeling approaches is the focus of this section. The first model uses a conservation of mass approach and is based on the work presented in (Higg and Wornyoh, 2008), (Danyluk and Dhingra, 2012a). A third-body mass transfer concept is applied to account for the transport of the film from the ball surface to the rod and race contact surfaces as seen experimentally in Figures 8 and 9. The second modeling approach is similar to the Lundberg-Palmgren model in that the RCF data from the test configurations of Table 1 are used to fit a load-capacity parameter, C, to L_{10} data similar to that found in chapter 8 of (Bhushan, 1999).

4.1. Third body transfer model

The third-body model concept involves mass transfer of the solid film lubricant from its source to the contacting surfaces within the rolling-contact system. For example, if a specimen of silver that is stationary is pressed into contact with a rotating shaft the resulting contact will enable transfer of the soft silver from the specimen to the contact surface of the

shaft. The rate of silver transfer is related to: i) the force of the contact, ii) the surface roughness and speed of the shaft, and iii) the rate at which excess silver is pushed out of the contact area. Concerning the RCF tests in Figures 8 through 10, the source of the solid lubricant is the amount of thin-film coating on the balls at the beginning of the test, approximately 200 nm. The film lubricant is transferred to the rod and race contact areas, which are considered the third-body volumes. Depending on surface roughness, more or less lubricant may accumulate in the valleys between surface asperities on the rod and race surfaces. The solid lubricant on the ball surface represents the source or input to the third-body concept.

The control volume fraction coverage model (CVFC) has been presented and explained in (Higgs and Wornyoh ,2008), however, some parts of that formulation are presented here for clarity. The assumptions of the CVFC model for solid lubrication transfer to the third-body volumes are as follows: i) the ball/rod and ball/race contact surfaces are flat within their contact areas, ii) incipient sliding occurs between surfaces due to elastic deformation, iii) the fractional response and friction of the interfaces is primarily a function of the amount of silver present in the third-body volumes of the race and rod, and on the surface of the ball.

A conservation of mass formulation for the transfer of film lubricant from the ball surface to the wear tracks of the race and rod is as,

$$\begin{pmatrix} Third\ Body \\ Storage\ Rate \end{pmatrix} = \begin{pmatrix} Third\ Body \\ Input\ Rate \end{pmatrix} - \begin{pmatrix} Third\ Body \\ Output\ Rate \end{pmatrix}. \tag{1}$$

The output rate in equation (1) is driven by the load between the ball-rod and ball-race that forces some of the solid silver out of the wear track. Examination of the wear tracks on the races and on the rod and race in Figures 8 through 10 illustrate that silver is pushed outside of the CVFC volume over time, and hence removed from the third-body storage volumes. The input rate to the third-body storage volumes of the rod and race contact zones is influenced by the fiction coefficient between the solid lubricant and contact area. Concerning RCF contact and Figures 8 through 10, incipient sliding between the ball-rod and ball-race is assumed throughout this formulation.

Equation (1) may be described as the rate of change of the fractional coverage, $X(t)$ of the third-bodies on both the rod and race wear tracks. For the present study, $X(t)$ will be normalized to the average surface roughness of the race and rod as presented in Table 3, or approximately 250 nm and represents the maximum asperity height defined as, h_{max}. The asperity depth is about the same as the initial silver coating thickness on the balls as well, approximately 200 nm. Following the form of (Higgs and Wornyoh, 2008), and (Danyluk and Dhingra, 2012a) the fractional coverage variable is defined as,

$$X = \frac{h}{h_{\max}}, \tag{2}$$

where h is the local height of silver coating in the third-body volumes. Archard's volume wear rate law is used to account for surface wear interactions and is defined as,

$$\frac{dV}{dt} = KF_N U, \tag{3}$$

where V, K, F_N, and U are the volume, wear coefficient, normal force, and sliding velocity, respectively. The wear coefficient K is the probability that a surface is being worn due to sliding contact, and for this section incipient sliding assumed. Combining equations (1) through (3) gives the following differential equation for $X(t)$ as,

$$Ah_{\max}\frac{dX}{dt} = \left(K_{bc}F_cU_c + K_{br}F_rU_r\right)\left(1-X\right) - \left(K_{bEc}F_cU_c + K_{bEr}F_rU_r\right)X, \tag{4}$$

where the first term on the right hand side accounts for third body input and the second term for third body removal. The solution of Eq. (4) is given as:

$$X(t) = \frac{K_{bc}F_cU_c + K_{br}F_rU_r}{K_{bc}F_cU_c + K_{br}F_rU_r + K_{bEc}F_cU_c + K_{bEr}F_rU_r}\left(1-\exp\left(-\frac{t}{\tau}\right)\right). \tag{5}$$

The constants K_{bc} and K_{br} are the wear coefficients for silver between the ball-race and the ball-rod, respectively, and influence how the third body is filled with silver from incipient sliding during the test. The constants K_{bEc} and K_{bEr} are the wear coefficients for the silver that is pushed out of the wear track between the ball-race and ball-rod. The wear coefficients K_{bEc} and K_{bEr} influence how much silver is removed from the third-body due to ball sliding with the edge of the wear track during the test as shown in Figures 8 and 9. The time constant τ in equation 5 is defined as,

$$\tau = \frac{Ah_{\max}}{K_{bc}F_cU_c + K_{br}F_rU_r + K_{bEc}F_cU_c + K_{bEr}F_rU_r}, \tag{6}$$

and defines the time to steady state third-body thickness. It was found that τ also correlates with the run-in time of the RCF test configurations in Table 1. The condition $X(t) > 0$ signifies that silver is being transferred from the ball surface to the third-body volumes on the race and rod. When all of the silver has been transferred from the ball, the condition $X(t) = 1$ exists and the third body input rate goes to zero as defined in equation (4). As the third-body volume becomes depleted, that is, as silver is pushed out of the wear track as defined in the second term on the right hand side of equation (4), the test results of Figure 9 and Table 4 column 3 begins to occur. As soon as the input to the third-body volumes ceases, the volume coverage $X(t)$ diminishes resulting in asperity-to-asperity contact such that friction and vibration increase and the stopping threshold criteria of Section 2.3 is exceeded.

Equation (5) is plotted in Figure 11 using the material properties, wear coefficients, and loads presented Tables 2, 5, and 6. The wear coefficients presented in Table 5 are within the range and order of magnitude of those tested between bearing steels like Rex20 and silver, and those tested between Si_3N_4 and silver under UHV conditions found in references (Holmberg and Matthews, 2009) and (NASA/TM 1999-209088, 1999). Table 6 contains normal load and contact area calculations from the RCF test rig of Figure 2c and are used in the calculations of equations (5) and (6).

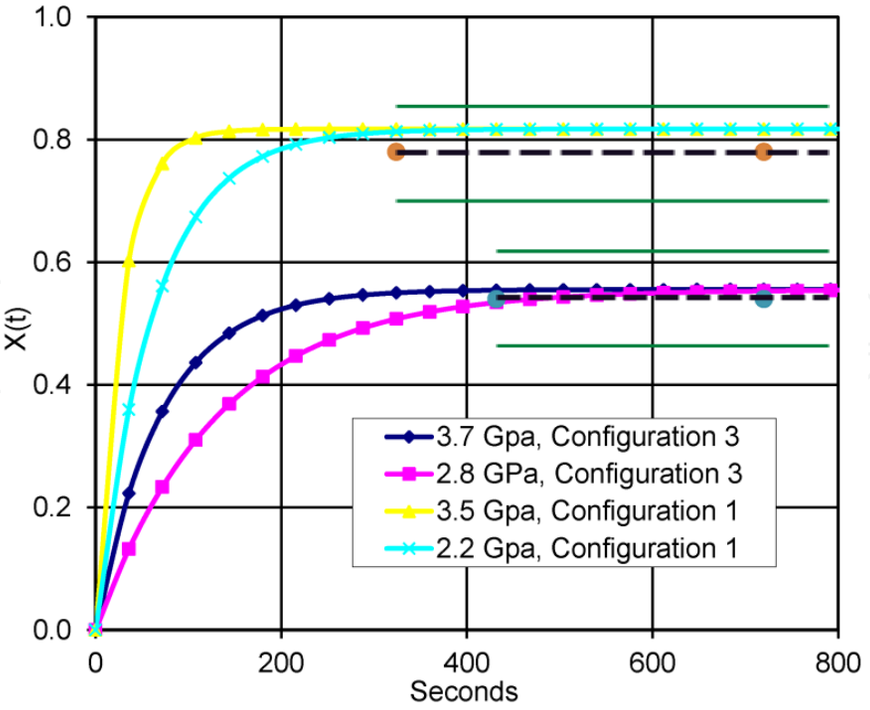

Figure 11. Fractional coverage of the third body volume calculated using equations (5) and (6) with values from Tables 2, 5, and 6 for two test configurations from Table 1.

K (m^2/N)	K_{bc}	K_{br}	K_{bEc}	K_{bEr}
Test Configuration 3	1.0E-15	2.0E-16	1.0E-15	5.0E-17
Test Configuration 1	1.0E-15	2.0E-15	1.0E-15	2.0E-17

Table 5. Wear coefficients used in equations (5) and (6).

Hertzian Contact Stress (GPa)		F_r (N)	F_c (N)	Third Body Surface Area (m^2)
Test Configuration 3	3.7	264	145	7.2E-05
	2.8	101	56	5.4E-05
Test Configuration 1	3.5	237	130	6.2E-05
	2.2	67	37	3.7E-05

Table 6. Normal forces and third-body contact area calculations.

Observation of the curves in Figure 11 suggests steady-state third-body coverage after 400 seconds of RCF testing. For comparison, thickness measurements of the silver remaining on the balls of suspended RCF tests reveal a third-body-coverage steady state value, X_{ss}, between 0.46 to 0.61 when testing in configuration 3 and, X_{ss} between 0.68 and 0.89 when testing in configuration 1. This data was collected from suspended tests similar to Figure 8 and do not include spall failures. These values represent a range of steady state fractional coverage for each configuration and are shown in Figure 11 as dashed lines with solid lines above and below indicating the range of measured coverage, X_{ss}.

Comparison of the measured steady state coverage, X_{ss} with that calculated from solution of equation (4) shows good agreement between measured and predicted third body fractional coverage using the wear coefficient values presented in Table 5. The trending of coverage, X_{ss}, to the same steady state values for each of the configurations 1 and 3 is due to the material type and loading conditions related to the RCF test setup. The run-in time for each of the test configurations 1 and 3 is comparable with the transient portion of the curves in Figure 11, suggesting that the volumes between asperities on the rod and races fill-up within the first 10 minutes of the test rotating at 130 Hz.

A steady state wear factor for the depletion of silver from the ball may be calculated using Archard's wear equation integrated over time as,

$$V_{ball} = \int_0^{t_f} K_{ball} F_{ball} U_{ball} \left(1 - X(t)\right) dt. \tag{7}$$

Solution of equation (7) and application of equation (5), the ball steady state wear factor may be expressed as,

$$\varphi = \frac{V_{ball}}{F_{ball} t_f U_{ball}} g, \tag{8}$$

where g is the gravitational constant and t_f is the time to failure based on the stopping threshold criteria 0.35g. Table 7 contains evaluation of Equation (8) using RCF depletion-failure data from Figures 6 and 7. Spall failures were not included in the wear factor calculations of Table 7. Configuration 2 shows the smallest wear factor and had the longest RCF test life. The wear factors of configurations 1 and 3 are about the same suggesting similar test-time results using either the Rex20 rod or the Si_3N_4 rod with 12.7 mm balls. The result that wear factors for configurations 1 and 3 are similar regardless of rod type suggests that most of the third-body storage volume resides on the race. This is confirmed from the autopsy results of Figures 9 and 10 in that silver has been pushed out of the wear track on the race.

Table 1 Test Configuration	Configuration 1		Configuration 2		Configuration 3	
Contact stress	3.5 GPa	2.2 GPa	4.1 GPa	3.5 GPa	3.7 GPa	2.8 GPa
Wear Factor $\left(cm^3 cm^{-1} kg^{-1}\right)$	3.47E-10	3.23E-10	7.49E-11	3.37E-11	3.12E-10	2.34E-10

Table 7. Steady state wear factor of the ball, calculated using data from all non-spall RCF tests.

4.2. Lundberg-Palmgren emperical model

Empirical modeling with ex-situ data allows coating life prediction based on past performance. RCF data collected over a range of contact stresses may be used to extrapolate

coating-life within the range of the stresses tested. In this section a Lundberg-Palmgren model is used to back-calculate a basic load capacity parameter, *C*, for each of the test configurations of Table 1. The load capacity parameter may then be used to plan the length of any UHV-RCF test based on the test-load for each configuration. The load capacity calculation follows (Bhushan, 1999) chapter 8. The stress cycles corresponding to 10% failure maybe calculated as,

$$L_{10} = \left(\frac{C}{W}\right)^3, \tag{9}$$

where the variable *W* corresponds to the radial load applied to the ball, and *C* is the basic load capacity of the test configuration with respect to a ball-bearing type system. The basic load capacity parameter, *C* may be calculated using the RCF cycles-to-failure results similar to those presented in Figures 5 through 7. The values of L_{10} and *W* were measured for each of the test configurations shown in Table 1. Using data from Table 6 the L_{10} life for each test configuration and loading is plotted as a function of load capacity in Figure 12. The measured L_{10} life for different contact stresses is also plotted in Figure 12 as well, represented as vertical lines (large and small dashed lines, and one dash-dot line).

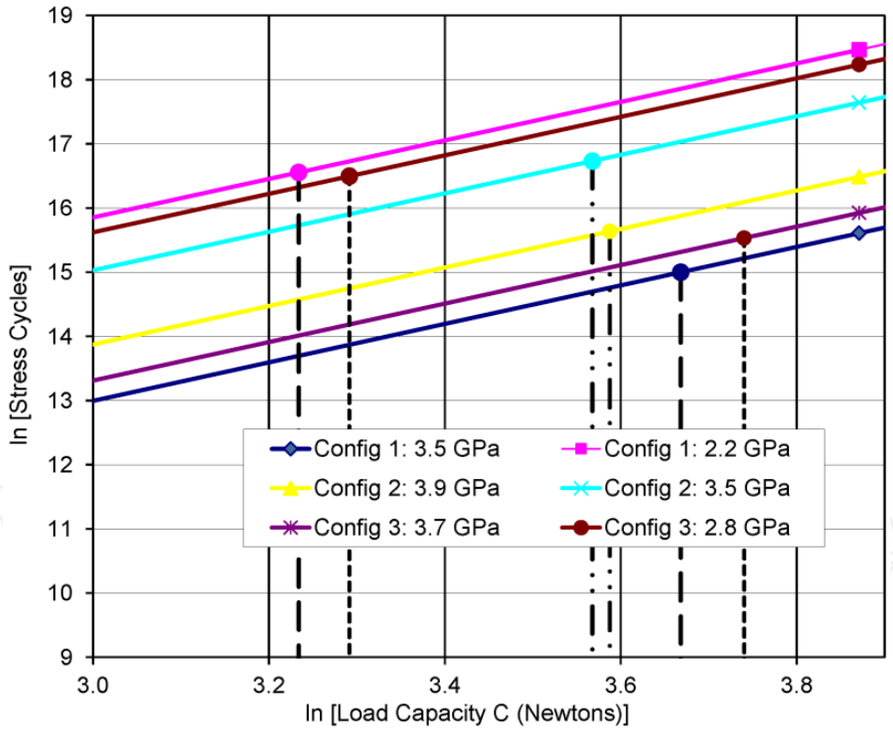

Figure 12. Plot of the natural log of L_{10} stress cycles verses load capacity parameter, *C*, using equation (9) for three test configurations in Table 1. Vertical lines represent measured L_{10} life for three test configurations and three loads (GPa).

The Lundberg-Palmgren model in equation (9) may require life-adjustment factors to fit the model to experimental data. Concerning Figure 12, it is to be expected that the load capacity parameter, *C*, will be the same for each test configuration independent of loading.

Configuration 2 demonstrates this attribute. The dash-dotted vertical lines related to configuration 2 are very near to each other, suggesting that life-adjustment factors are not needed to fit the data related to configuration 2. Equation (9) alone may be used to predict RCF life based on W and C when testing in configuration 2. In contrast, configurations 1 and 3 give different load capacity parameters for the same configurations as shown in Figure 12. The large and small dashed-lines related to Configurations 1 and 3 do not line up on the same load capacity parameter, C, suggesting that life-adjustment factors will be needed to accurately calculate L_{10} life for these test element combinations.

5. Conclusions

A ball-rod RCF test platform has been successfully demonstrated for testing thin solid film lubricants in ultra-high vacuum and at high rotational speeds. The film systems tested included silver and nickel-copper-silver and results indicate that film thickness initially present on the balls has the most influence over test life based on 118 tests and a thickness range of 180 to 200 nm. The Weibull shape factor for all test data was in the range of 2.5 to 2.8, indicating typical bearing-type failure modes and test-times. A shape factor in this range suggests predictability of the test method, which enables repeatable conclusions concerning tribology testing of rolling bearing elements.

For the two ball sizes investigated, the 7.94 mm ANSI T5 balls with nickel-copper-silver gave longer RCF test life than the 12.7 mm M50 steel balls for similar Hertzian contact stress loading. Surface finish of the balls and races also influenced test longevity, with longer life and higher load capability for the 7.94 mm T5 balls with a surface Ra of 0.04 compared to the 12.7 mm M50 balls with a surface Ra of 0.32. The surface roughness of the races directly affects the volume of silver that may be stored within the wear track over the course of the test. Rod material and surface finish did not influence test time for the materials Rex 20 steel and Si_3N_4.

Two types of failure modes were observed for all tests: i) early spall failure and, ii) silver film depletion. In the former, a film-spall on at least one ball resulted in increased friction and plastic yielding within the contact area leading to the onset of spall at the ball-film interface. In the latter failure mode, as the lubricant film became depleted the friction and vibration increased and the test was stopped.

Surface finish of the rod and race elements influences the rate of solid film transfer from the ball surface to the rod and races. Inspection of the wear surfaces of suspended test components suggested a third-body transfer mechanism of the lubricating film could be used to predict test longevity. A third-body self-replenishing model approach was applied and there is good agreement with measured steady state film thickness and predicted film height.

A Lundberg-Palmgren empirical model fit of the RCF test data for L_{10} life was used to calculate the load-capacity parameter for three test configurations. Stable prediction of a load capacity parameter will enable better planning for expanded used of the UHV-RCF test platform. The load capacity parameters for configurations involving 12.7 mm M50 balls with M50 races varied with applied load, suggesting that further work is needed to establish load-reduction correction factors for these configurations. Load-reduction factors for

configurations involving 7.94 mm T5 balls with nickel-copper-silver film are not required. Future work with the UHV-RCF platform will involve continued testing for influence of process parameters and deposition methods, such as magnetron, on RCF test life similar to Danyluk and Dhingra (2011, 2012a). Expansion of the platform for study of surface interaction with heat and fatigue under high vacuum will also be explored.

Author details

Mike Danyluk* and Anoop Dhingra
Mechanical Engineering Department, University of Wisconsin Milwaukee, Milwaukee, Wisconsin USA

6. References

Berthier Y, Godet M, Brendle M, (1989), Velocity accommodation in friction, *Tribology Transactions*, 32: 490-496.

Bhushan B, (1999), Principles and Applications of Tribology, *John Wiley & Sons, New York*, Chapters 4 and 8.

Danyluk M, Dhingra A, (2011), Rolling Contact Fatigue in High Vacuum Using Ion Plated Nickel-Copper-Silver Solid Lubrication, *J. Vac. Sci. Technol. A*, 29: 011005.

Danyluk M, Dhingra A, (2012a), Rolling contact fatigue using solid thin film lubrication, *Wear* 274-275: 368 - 376.

Danyluk M, Dhingra A, (2012b), Influence of process parameters on rolling-contact-fatigue life of ion plated nickel- copper-silver lubrication, *J. Vac. Sci. Technol. A*, 30: 031502.

Higgs C, Wornyoh E., (2008), An in situ mechanism for self-replenishing powder transfer films: Experiments and modeling, *Wear* 264: 131-138.

Holmberg K, Matthews K (2009) Coatings Tribology Properties, Mechanisms, Techniques and Applications in Surface Engineering, Volume 10: 202-208, Elsevier.

Hoo J, (1982), A Ball-Rod Rolling Contact Fatigue Tester, *ASTM STP 771 ASTM* pp.107-124.

Hu Y, Zhu D, (2000), A Full Numerical Solution to the Mixed Lubrication in Point Contacts, *Journal of Tribology*, Vol. 122, Issue 1, pp.1-9.

Matthews A, Franklin S, Holmberg K, (2007), Tribological coatings: contact mechanisms and selection, *J. Phys. D: Appl. Phys* 40: 5463-5475.

NASA report SP-5059(01), (1972), Solid Lubricants: A Survey, Technology Utilization Office NASA.

NASA/TM 1999-209088/Part1, (1999), Friction and Wear Properties of Selected Solid Lubricating Films, Part 1: Bonded and Magnetron-Sputtered Molybdenum Disufide and Ion-Plated Silver Films.

Polonsky I, Chang T, Keer L, Sproul W, (1998), A Study of rolling contact fatigue of bearing steel coated with PVD TiN films: Coating response to cyclic contact stress and physical mechanisms underlying coating effect on the fatigue life, *Wear* 215: 191-204.

* Corresponding Author

Rosado L, Forster N, Thompson K, Cooke J, (2010), Rolling Contact Fatigue Life and Spall Propagation of AISI M50, M50NiL, and AISI 52100, Part 1: Experimental Results, *Tribology Transactions*, 53: 29-41.

Sadeghi F, Jalalahmadi B, Slack T, Raje N, Arakere N, (2009), A Review of Rolling Contact Fatigue, *Journal of Tribology*, Vol. 131, Issue 4, pp.1-15.

Wornyoh E, Higgs C, (2011), An asperity-based fractional coverage model for transfer films on a tribological surface, *Wear* 270: 127-139.

IntechOpen